Journal of
Materials Chemistry C

Accepted Manuscript

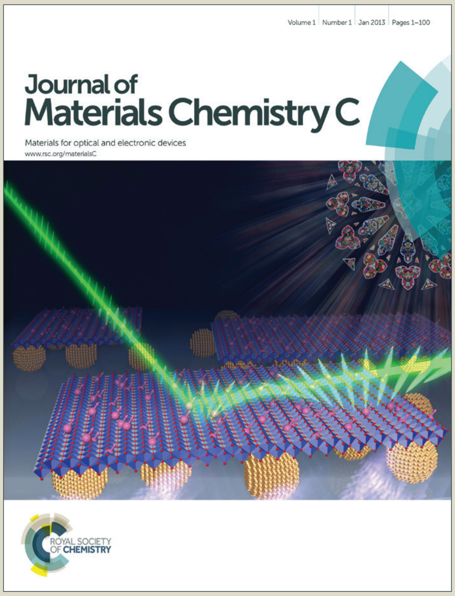

ROYAL SOCIETY
OF CHEMISTRY

www.rsc.org/materialsC

Journal of Materials Chemistry C RSCPublishing

ARTICLE

Cite this: DOI: 10.1039/x0xx00000x

Self-assembly of metal ions induced highly emissive fluorophore-triphenylamine nanostructures: enhanced two-photon action cross section for bioimaging applications

Received 00th January 2012,
Accepted 00th January 2012

DOI: 10.1039/x0xx00000x

www.rsc.org/

Lin Kong,[a] Yu-peng Tian*,[a,b,c] Qi-yu Chen,[a] Qiong Zhang,[a] Hui Wang,[a] Dong-qin Tan,[a] Zhao-ming Xue,[a] Jie-ying Wu,[a] Hong-ping Zhou,[a] and Jia-xiang Yang*[a,b]

A D-π-A type triphenylamine derivative (E)-3-(4-(4-(diphenylamino)styryl)-phenyl)acrylonitrile (abbreviated as **L**) is designed, synthesized and characterized by single crystal X-ray diffraction analysis, which is demonstrated to exhibit superior AIEE (aggregation-induced enhanced emission) properties. Self-aggregates of **L** obtained with and without the guidance of metal ion (Cd^{2+} or Cu^{2+}) showed morphology-dependent luminescent properties. The coupling and synergy effects between **L** and metal ions bring about an energy transfer process between the components, which further result in red-shifted absorption and fluorescence, enhanced fluorescent quantum yield, tunable FL lifetime. The interactions between **L** and metal ions also change nonlinear optical properties, including two-photon excited fluorescence (2PEF), two-photon absorption (2PA) cross section (δ), two-photon action cross section ($\eta\delta$) and two-photon absorption coefficient (β), which further make the samples successfully apply to a two-photon fluorescent probe for labelling the intercellular section. The study indicates that the preparation of nanohybrids from metal ions and AIEE organic compound is a promising method to prepare 2PA probes possessing high ηδ for biological imaging.

1. Introduction

In the past few decades, two-photon absorption (2PA) has gained increasing interest for its promising applications in biological fields, such as bio-target sensing [1], two-photon excited fluorescence microscopy [2], and high-resolution three-dimensional imaging of biological systems [3]. Compared with traditional single-photon fluorescence imaging, two-photon fluorescence imaging techniques have shown many advantages, such as generating high-energy fluorescence from low-energy irradiation, deeper-tissue penetration, lower interference from autofluorescence and self-absorption, minimal phototoxicity and photobleaching to living biosubstrates [4], and so forth. The applications highly rely on the 2PA cross-section and two-photon emission fluorescence (2PEF) of the specifically engineered materials. To fully realize application of two-photon fluorescence imaging, good two-photon probes with large two-photon action cross-section (equivalent to ηδ, where η is the fluorescence quantum yield, δ is the 2PA cross section) at desirable wavelengths in biological media remain in urgent demand.

There are many types of materials with large ηδ value, such as π-conjugated dipolar, quadrupolar, and octupolar molecules [5], coordination compounds [6], ultra-small fluorescent metal nanoclusters [7]. Among these classes of 2PA materials, organic 2PA chromophores have attracted great interests due to their feasible preparation and abundant versatility [8]. However, the ηδ values of these organic soluble 2PA materials commonly show sudden decrease in aqueous media, which is mainly caused by notoriously known aggregation-caused fluorescence quenching (ACQ) due to π-π stacking and other nonradiative pathways [9]. In this regard, organic chromophores with aggregation-induced emission (AIE) and/or aggregation-induced enhanced emission (AIEE) signature [10] provide a useful way to solve this problem.

Typical AIE fluorogens are weak or non-emissive in dilute solution but become highly luminescent in the aggregated state, due to the restriction of their intramolecular rotations by intermolecular steric interaction in the aggregate state, which opens the radiative pathway [11]. As is known that, the aggregation degree determines the fluorescence intensity and the corresponding ηδ value of the material [12]. Thus, obtaining stable aggregation structure is a main key to enlarge the ηδ value of these chromophores. There are many ways to increase the aggregate degree of an AIE chromophore, such as altering the water fractions in the preparation procedure [13], adjusting the concentration of the dye [14], changing the fabrication methods including drop casting, recrystallization, vacuum evaporation, and spin coating [15], changing the preparation solvent to alter the weak interactions among the studied system [16], packing layers of chromophores as a shell on inorganic nanoparticle core [17], and so on. The mechanism of the enhanced ηδ value relates to the increased concentration of the chromophores at a particular location, the intermolecular interactions between chromophores themselves and/or between chromophores and the surroundings, among which the latter was much important as they can also change the aggregate state of the chromophore to some extent. Such intermolecular interactions contain hydrogen bonding, π-π and/or C-H···π stacking interactions, van der Waals, electrostatic interactions, which are very important to tune the factors influencing the self-assembly process and the corresponding final morphology [18]. The dominant interactions only occur at the liquid-liquid or liquid-solid interfaces. Thus, the nature of the chromophores and the additive substance in the solution are the main keys to adjust the intermolecular interactions, which further change the aggregates degree of an AIE chromophore and the corresponding ηδ value. The additive substance in the solution include surface active agent, acid-base balance ions, anions [19], different valent metal ions that can bring about strong binding and complexation between the metal ions and the studied chromophore [20]. However, to the best of our knowledge, the fabrication of metal ions induced organic micro- and/or nanostructures through covalent and/or noncovalent interactions to increase the aggregates degree of an AIE chromophore and further adjust the corresponding 2PA action cross section is rarely reported.

Considering all the above aspects, we describe herein an AIEE type 2PA fluorogen, (E)-3-(4-(4-(diphenylamino)styryl)-phenyl) acrylonitrile (abbreviated as **L**), and the fabrication of the corresponding **L** nanoaggregates with different aggregate degree self-assembled in water for labelling HepG2 cells. Triphenylamine group was used as electron donor unit and attached to the C=C double bond and benzene group to construct the activator for AIE. Then, cyano group was used as electron acceptor unit to construct **L** as a D-π-A type molecule endowing **L** with both intramolecular charge transfer (ICT) feature and AIEE behaviour [21]. Further studies revealed that **L** exhibited square-like morphology in EtOH-H_2O mixed solution while wire-like and spherical morphology was obtained with the participation of cadmium and copper ion, respectively, which exhibited higher aggregate degree and higher ηδ value than **L** square obtained without metal ions. The mechanism was associated with the intermolecular interactions between **L** and cadmium/copper ions, which changed the growth direction, aggregate degree, the electronic structure, ICT process of **L** molecules and brought about energy transfer between the components, thereby altered the linear optical properties (including red-shifted UV absorption and fluorescence wavelength, enhanced fluorescent quantum yield, tunable FL lifetime) and non-linear characteristics (including increased δ value, increased ηδ value, changeable 2PEF intensity, enhanced third-order nonlinear susceptibility). The existence of metal ions and enlarged 2PA properties were important to their 2PFM bio-imaging applications in HepG2 cells, labelling the intercellular section.

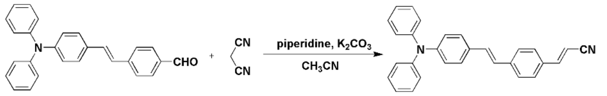

Scheme 1 The synthetic routes for **L**

2. Experimental

2.1. Preparation of L

L was synthesized through reported literature [22]. In detail, (E)-4-(4-(diphenylamino)styryl)benzaldehyde (0.38 g, 1 mmol), dicyanomethane (0.08 g, 1.2 mmol), potassium carbonate (0.69 g, 5mmol) and piperidine (0.42 g, 5 mmol) were dissolved in acetonitrile (50 mL), refluxed overnight and monitored by TLC. The reaction mixture was then poured into CH_2Cl_2 (500 mL), washed with water (100 mL × 4) and dried over $MgSO_4$. The solvent was evaporated, and the residue was purified by column chromatograph of silica gel with ethyl acetate/petroleum ether mixture (1:50 v/v) as the eluent. Thus, **L** was obtained as a light yellow solid. ^1H NMR (400 MHz, $CDCl_3$) δ (ppm): 7.64 (m, 5H); 7.53(d, 2H, J = 8.0 Hz); 7.35 (s, 1H); 7.33 (s, 2H); 7.32 (d, 2H, J = 7.6 Hz); 7.14 (d, 1H, J = 16.4 Hz); 7.09 (t, 4H, J = 8.4 Hz); 7.02 (d, 2H, J = 8.4 Hz); 6.96 (d, 2H, J = 8.4 Hz); 6.45 (d, 1H, J = 16.8 Hz). *Anal. Calc.* for $C_{29}H_{22}N_2$: C, 87.41, H, 5.56, N, 7.03, Found: C, 87.20, H, 5.59, N, 6.75 %.

Light yellow crystals of **L** suitable for X-ray diffraction were obtained by slow evaporation of acetonitrile solution at room temperature for about 2 weeks.

2.2. Preparation of L wires and L spheres

L-EtOH solution (200 μL of 1.0 × 10^{-3} mol/L) was injected into 20 mL of high-purity aqueous solution of $Cd(NO_3)_2 \cdot 4H_2O$ (1.0 × 10^{-5} mol/L) or $Cu(NO_3)_2 \cdot 3H_2O$ (1.0 × 10^{-5} mol/L) under stirring. The mixture was stirred for 10 min and then left undisturbed overnight at room temperature for stabilization. Then, the precipitate was centrifugated, washed with distilled water several times to remove excess inorganic salt and EtOH, and then dispersed into high-purity water, and the above solution was used for characterization and analysis.

Comparative experiments were also carried out. Free **L** nanocrystals were prepared through the corresponding similar process in the absence of metal ions. For studying the effect of solvents on the aggregation of **L**, ethanol, tetrahydrofuran (THF) and N,N-dimethyl formamide (DMF) were used as the solvent. In detail, **L**-EtOH solution, **L**-THF solution and/or **L**-DMF solution was injected into high-purity water, respectively. To study the effect of concentration, different dose of **L**-EtOH solution was used to get 1.0 × 10^{-5}, 2.0 × 10^{-5}, 3.5 × 10^{-5} and 4.0 × 10^{-5} mol/L of **L**, respectively.

2.3. Nonlinear optical measurements

The nonlinear optical properties of **L** squares, **L** wires and **L** spheres were measured through Z-scan measurement and two-photo-excited fluorescence (2PEF) with a concentration of 1.0 × 10^{-4} mol/L (based on Mol. Wt. of **L**) using femtosecond laser pulse and Ti:95 sapphire system (10 Hz, 140 fs). For 2PEF measurements, quartz-glass sample with 1.0 cm thickness were used. While for Z-scan measurements, the quartz-glass cell was 1.0 mm thick, and the average laser power was 36 mW. The optical path length for Z-scan was 5.0 cm from the sample.

Nonlinear absorption coefficient β was measured by open aperture Z-scan technique. For the open aperture, the normalized transmittance as a function of the position along the z axis can be written as **equation 1**

$$Tz = \sum_{m=0}^{\infty} \frac{[-q(z)]^m}{(m+1)^{3/2}}, \text{ where } q(z) = \frac{\beta I_0 L_{eff}}{[1+(z/z_0)^2]\alpha} \qquad \mathbf{(1)}$$

Z_0 was the diffraction length of the beam, I_0 was the intensity of the light at focus, L_{eff} was the effective length of the sample, α was the linear absorption coefficient at the wavelength used.

Further, the molecular 2PA cross-section (δ) could also be determined through Z-scan measurement by using the following relationship, **equation 2**,

$$\delta = h\upsilon\beta \times 10^{-3}/N_A d, \qquad \mathbf{(2)},$$

where h was the Planck's constant, υ was the frequency of input intensity, N_A was the Avogadro constant, and d was the concentration of the sample.

2.4. Cell culture, incubation and 2PFM imaging

HepG2 cells were seeded in 6 well plates at a density of 2 × 10^5 cells per well and grown for 96 hours. For live cell imaging, cell cultures were incubated with the chromophores (10% PBS: 90% cell media, PBS = phosphate buffered saline) at a concentration of 20 μM and maintained at 37 ºC in an atmosphere of 5% CO_2 and 95% air for incubation times ranging up to 30 min. The cells were then washed with PBS (3 × 3 mL per well) and then 3 mL of PBS was added to each well. The cells were imaged using confocal laser scanning microscopy and water immersion lenses. All of the experiments were repeated three times; the measured data for each set of experiments were expressed with the average value.

HepG2 cells were fluorescence imaged on a Zeiss LSM 710 META upright confocal laser scanning microscope using 40 × magnification water-dipping lenses for the monolayer cultures. Image data acquisition and processing was performed using Zeiss LSM Image Browser, Zeiss LSM Image Expert and Image J.

2.5. Instruments

The X-ray diffraction measurement of single crystal was performed on a Bruker SMART Ⅱ CCD area detector using graphite-monochromated Mo Ka radiation (k = 0.71073 Å) at 296(2) K. Intensity data were collected in the variable multi-scan mode. The structures were solved by direct methods and difference Fourier syntheses. All non-hydrogen atoms were refined anisotropically and hydrogen atoms were introduced geometrically. Calculations were performed with the SHELXTL-97 program package [23]. Field emission scanning electron microscope (FE-SEM) was performed on JEOL JSM-4800 scanning electron microscope. TEM was performed on JEOL JEM 2100 high-resolution transmission electron microscope operated at 300 KV. Fourier transform infrared (FT-IR) spectra were recorded on a Nicolet-780 FT-IR instrument with samples prepared as KBr pellets. The Raman spectra were recorded with a Labram-HR spectrometer using the 325 nm line of the Ar ion for excitation. Ultraviolet-visible (UV-vis) absorption spectra were obtained with a Hitachi UV-3100 UV-VIS-NIR spectrophotometer. Photo-luminescence (PL) spectra were collected on Hitachi F-7000 fluorescence spectrophotometer at room temperature. Fluorescence lifetime and fluorescence quantum yield measurements were carried out using an HORIBA FluoroMax-4P fluorescence spectrometer equipped with a time-correlated single-photon counting (TCSPC) card.

3. Results and Discussion

3.1. AIEE performances and morphology of L nanoaggregate

The absorbing and fluorescent properties of **L** nanoaggregates were investigated through a solvent-nonsolvent test, which is commonly used in the study of AIE/AIEE behaviour. As for **L**, EtOH is a good solvent and water is a poor solvent. Adding water to **L**-EtOH solution will cause the well-dissolved molecules to aggregate. The effects of water volume fraction (f_w) on the UV-vis absorption and fluorescence were evaluated in water/EtOH mixed media. The concentration of compound **L** was kept at 1.0×10^{-5} mol·L^{-1}.

The UV-vis absorption spectrum of **L**-ethanol solution exhibited two major absorption peaks at 304 nm and 402 nm (**Fig. 1a**), respectively. The latter corresponded to the π-π* transition of the whole π-conjugated **L** molecule, while the former resulted from the π-π* transition of triphenylamine fragment [24]. With an increasing content of water from 0 to 85 vol%, the absorption band of triphenylamine fragment remained at the same position, in general. However, with up to 60% volume fractions of water addition, the maximum absorption band of the whole π-conjugated molecule red-shifted to 404 nm compared with that of dilute **L**-EtOH solution, strikingly engender a rapid red-shift within the range of 65%~85% (λ_{abs} = 422 nm when f_w = 85%). The phenomenon may mainly result from the extension of the effective conjugated lengths caused by the planarization of a twisted molecule in the aggregate state. This bathochromic effect also indicated the formation of J-aggregate exhibiting enhanced emission as compared to the face-to-face (or sandwich-like) H-aggregate [25]. The formation of aggregate was deduced from the lifted level-off tail in the absorption spectra of **L** when the water volume fraction was 65% to 85% (**Fig. 1a**). These tails in the visible region were attributed to Mie scattering caused by nanosized particles [26]. However, when $f_w \leq 60\%$, no such tail was observed because **L** was fully dispersed.

The compound **L** in EtOH solution emitted yellow light under illumination at the concentration of 1.0×10^{-5} mol·L^{-1} with a 365 nm UV lamp (insert in **Fig. 1c**), the emission band of which was 546 nm. Upon gradual addition of water into EtOH solution (**Fig. 1b**), the fluorescence of **L** was continuously red-shifted as well as reducing its quantum yield at the initial stage, which was mainly attributed to the increase in solvent polarity, the intramolecular charge transfer (ICT) effect and/or twist intramolecular charge transfer (TICT) effect [27]. The emission band showed a largest red-shift as f_w = 40% with λ_{em} = 565 nm (**Fig. 1b-c**).

The fluorescence intensity showed ~80% decrease as f_w = 50% (**Fig. 1b-c**), after which the fluorescence intensity increased and the emission colour was gradually blue-shifted with further addition of water up to 85% under the same processing conditions with λ_{em} = 536 nm and 12 times enhanced intensity, indicating the AIEE

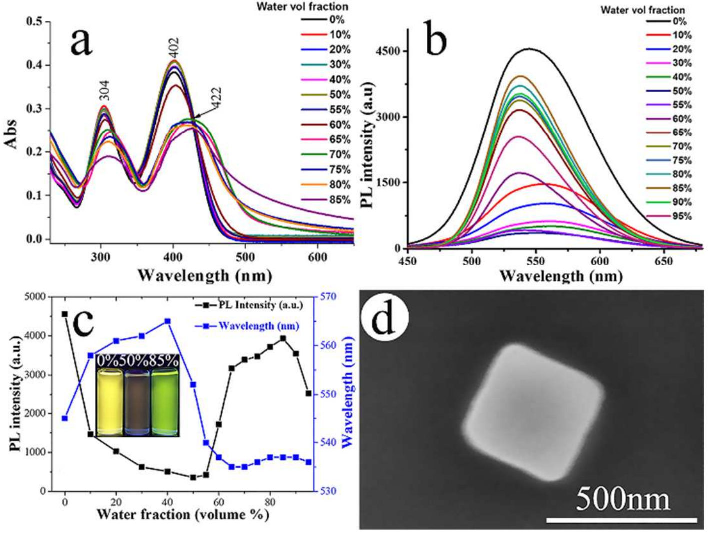

Figure 1. a) UV-vis absorption and b) PL emission spectra changes of **L** in EtOH-H$_2$O mixtures with different water volume fractions, c) the effect of water volume fraction (f_w) on the maximum emission intensity and emission wavelengths of **L** in EtOH-H$_2$O. Insets: **L** in 0%, 50% and 85% water under illumination at 365 nm. The concentration of **L** was 1.0×10^{-5} mol·L^{-1}, d) SEM image of **L** nanosquare prepared from EtOH-H$_2$O solution (f_w = 85%).

characteristic of **L** [27]. The fluorescence quantum yield of **L** at f_w = 85% was 0.33 and green-yellow light was observed with a 365 nm UV lamp (insert of **Fig. 1c**). As described above, the increasing polarity of the solvents and TICT effect led to the decrease in emission intensity and red-shift. Thus, the blue-shifts and enhanced emission in the EtOH-H_2O solution with 55% $\leq f_w \leq$ 85% may be attributed to the formation of crystalline aggregates [28]. However, the aggregates formed in aqueous mixtures with very high water content (> 85%) emitted only weak luminescence. When f_w > 85%, the molecules rapidly aggregated, the precipitate formed more quickly and amorphous aggregate appeared resulting in decreased emission [29], which also brought about disordered UV-vis absorption spectrum. Consequently, the varieties of the emission band and intensity may result from three factors: aggregate style, TICT effect and the corresponding solvatochromism.

Based on the experiments mentioned above, it can be concluded that **L** molecules tend to form crystalline aggregate when f_w is varied from 55% to 85%. Thus, SEM analysis was carried out to study the crystalline self-aggregate. **L** nanoaggregates were simply prepared without addition of any template, catalyst and/or surfactant by addition of **L**-solution to water (f_w = 85%) with vigorous stirring at room temperature for 10 min and then left undisturbed overnight for stabilization. Yellow fluorescent precipitates were found to appear in this process, which implied the formation of some sort of organized structure [30]. From SEM analysis, self-assembly aggregate of a regular square structure with the side length of ~400 nm and angle being close to 90º was presented as shown in **Fig. 1d**. The well-arranged organization revealed the crystalline self-aggregate of **L** molecules in this condition.

3.2. Crystal structure of L and mechanisms of emission enhancement

In order to better understand the relationship between the photophysical properties and the molecular packing, single crystal of **L** was prepared through slow evaporation of acetonitrile solution at room temperature. In the molecular structure of **L**, there were two molecules gathered together in a unit cell as shown in **Fig. 2**.

The adjacent molecules of **L** were stacked through C-H···π weak interactions (d = 2.816 Å), C27-H27···N4 weak interactions (d = 2.744 Å), C56-H56···N3 weak interactions (d = 2.813 Å) and/or C34-H34···C38 weak interactions (d = 2.881 Å) within the aggregated structure as shown in **Fig. S1-2**. Furthermore, the relative far center-to-center distance of pairs of molecules was 10.228 Å (**Fig. S1**). In this circumstance, the π-π stacking interaction was weakened and cannot cause the quenched emission.

We can conclude that the slipped-parallel structure not only avoids the maximum face-to-face stacking that causes the quenched emission, but also favours the dipole-dipole interactions in the ICT compound, and that the dipole-dipole interactions are the main driving force for dimer formation, which also lock the intermolecular rotations of the phenyls. Thus, the excited-state energy consumed by intermolecular rotation was greatly reduced, and enabled **L** to emit intensely in the aggregate state. The high conjugation mentioned above and the J-type aggregate equally resulted in the increase of the fluorescence intensity in the crystalline aggregate state.

Furthermore, the crystal data helped us to estimate the optical properties based on bond-length alternation (BLA) principle [31], which had been established as a useful parameter in relation to nonlinear optical response. The BLA across the π-bridge of **L** was 0.14 Å, indicating that there was a high delocalization system within the molecule and that **L** was an excellent NLO material.

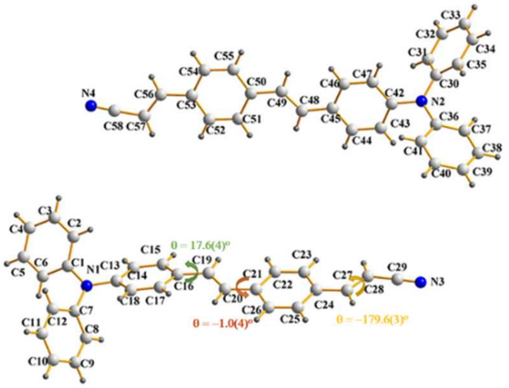

Figure 2 Crystal structure of **L** showing two molecules in a unit cell and some torsion angles

3.3. Morphology variation of L with the participation of Cd^{2+} and Cu^{2+} ions

After detailed investigation on free **L** aggregate, metal ion participated self-aggregate of **L** under the guidance of Cd^{2+} and/or Cu^{2+} was further studied. The concentration of **L** was kept as 1.0×10^{-5} mol·L^{-1}, equaling to that of metal cations and that in the experiments mentioned above. In the present case, the electrostatic attraction between Cd^{2+}/Cu^{2+} and the rich-electronic unit of **L** affected the molecular aggregate way and self-assembly process of **L** molecules. Consequently, violent changes of morphology were observed. The wire-like and spherical structures were obtained from EtOH-H_2O mixed solution containing **L**, $Cd(NO_3)_2$ or $Cu(NO_3)_2$, respectively, with no addition of any other materials. Some other metal ions were also used to study the evolution of the morphology, but only mint changes were captured. Under the guidance of Cd^{2+} ions, crystalline wires with a smooth surface (**Fig. 3a**) were clearly observed, the length of which was up to several tens of micrometers and the width varied from tens to hundreds of nanometers. The wire-like morphology was different from that of pure **L** and/or pure $Cd(NO_3)_2$ (see ESI† **Fig. S13**). The morphology changing from regular square structure to crystalline wire revealed that Cd^{2+} ions violently affected the aggregate pattern and/or growth direction of **L**. In this case, the electrostatic attraction between Cd^{2+} and the electronic-rich conjugated system of **L** molecule was the main driving force to change the morphology, which was resulted from the XRD experiment shown in ESI† **Fig. S10**. Furthermore, the comparison of Raman spectra of **L** squares and **L** wires clearly showed the down-shift in stretching vibration of the in-plane ring C-H bend changing from 1183 cm^{-1} for **L** square state to 1169 cm^{-1} for **L** wire. While the H bending frequency changed from 1263 cm^{-1} for **L** square to 1246 cm^{-1} for **L** wire [32]. Moreover, it can also be observed that the main vibrations at 1617 cm^{-1} of **L** square, which assigned to the ring C-C stretching vibration, slightly down-shifted to 1613 cm^{-1} of the **L** wire. The peaks at 1339 cm^{-1}, assigned to the

N-ph stretching, slightly down-shifted to 1336 cm^{-1} [33]. At the same time, it was also observed from FT-IR (**Fig. S12**) that the band at 2214 cm^{-1} attributed to the υ(C≡N) stretching vibration [34] did not change. The results suggested the strong binding took place between Cd^{2+} ions and the π-conjugated groups of **L** molecules. As **L** is a D-π-A type ICT compound, the interactions between **L** and Cd^{2+} ion can influence the ICT process of **L** molecule. The ICT degree of **L** molecule was stronger at this condition and the electrostatic attraction may enlarge the intermolecular interactions of **L** molecules along one direction and thereby resulted in the prolonged wires [6a]. The result of XRD (ESI† **Fig. S10)** also meant that when Cd^{2+} ions were used, the (011) reflection of **L** was the main diffraction.

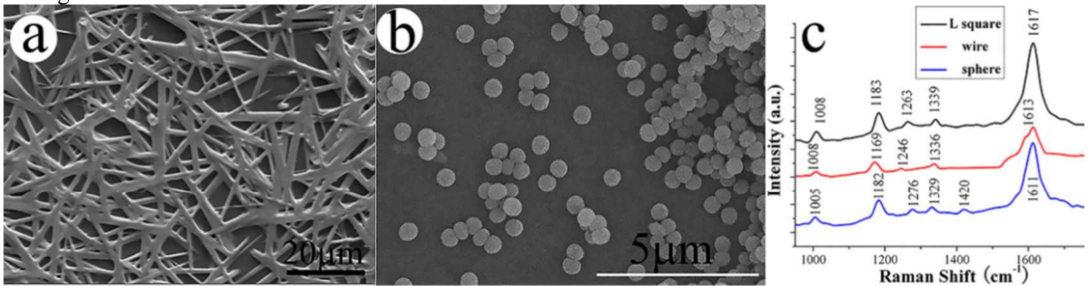

Figure 3. SEM images of (a) **L** wires, (b) **L** spheres, The concentration was 1.0×10^{-5} $mol \cdot L^{-1}$. (c) A comparison of Raman spectra of **L** squares, **L** wires and **L** spheres.

It is worth noting that the choice of metal ion can remarkably alter the morphology. With the participation of Cu^{2+} ion, monodispersed spherical particles (**Fig. 3b**) were observed, the size of which was about 400 nm. The morphology changing from regular square structure to spherical particles revealed that Cu^{2+} ions violently affected the aggregated pattern of **L**, which was very different from that of Cd^{2+} ions. The intrinsic morphology of $Cu(NO_3)_2$ showed a spherical aggregate tendency (**Fig. S14**), which meant that Cu^{2+} ions took part in the formation of the spherical particles of **Fig. 3b**. The XRD patterns (ESI† Fig. S12) revealed that when Cu^{2+} ions existed, the diffraction peaks were weakened and broadened, and several diffraction peaks appeared which corresponded to different diffraction plane.

Some differences between the Raman and FT-IR spectra of **L** square and **L** sphere were also observed in **Fig. 3c** and **Fig. S12**. The Raman band at 1617 cm^{-1} and 1339 cm^{-1} for **L** square slightly down-shifted to 1611 cm^{-1} and 1329 cm^{-1} for **L** sphere, respectively. Also, the band at 1263 cm^{-1} for **L** square up-shifted to 1276 cm^{-1} for **L** sphere. Notably, there appeared a new band centered at 1420 cm^{-1}, which was assigned to the N-ph+ ring vibration [33], which revealed that Cu^{2+} ion interacted with N atom of triphenylamine group. It was also observed from FT-IR that the band 2214 cm^{-1} attributed to the υ(C≡N) stretching vibration down shifted to 2089 cm^{-1}, which revealed that Cu^{2+} ion also interacted with C≡N group of **L** molecule. The results mentioned above clearly revealed that the coupling interactions between **L** and Cu^{2+} ion took place through the π-configuration unit, C≡N group and N atom of triphenylamine group. The phenomenon was reasonable that Cu^{2+} ion should have a tendency to combine with N atom, according to Hard-Soft Acid-Base principle. Thus, Cu^{2+} can interact with **L** at the both ends. In this case, the coupling effect occurred between Cu^{2+} and the electronic-rich conjugated system of the whole **L** molecule, along with the electrostatic interactions between *d* orbitals of Cu^{2+} and lone pair electrons of N atoms of both triphenylamine fragment and cyano unit. Thus, Cu^{2+} interacted with **L** at the both ends and induced **L** molecules uniformly grew along different directions and then gave rise to a spherical structure. This observation also revealed differences in the metal ions induced influencing of ICT process and the corresponding different long-range ordered supramolecular assembly leading to different mesoscopic structures.

As discussed above, there are two types of weak intermolecular interactions within the system, one is between adjacent **L** molecules that responsible for the molecular packing, the other is between metal ions and **L** molecules that can induce the oriented packing of **L** molecules. The existence of metal ions changed the shape of **L** aggregates due to different interaction 'hot spot' and the corresponding different growth direction. Further studies confirmed that Cd^{2+}, Cu^{2+}, in the form of ions, became part of the shape which were embedded in **L** wires and **L** spheres, respectively, as shown in ESI† **Fig. S15**. The existence of ions in the shape of **L** changed the growth direction, enhanced the aggregate degree and influenced the ICT process of **L** molecule, which can further bring about the changes of optical properties that closely linked with these two factors.

3.4. Linear optical properties

The long-range ordered organization at the nano- and/or micrometer scale is important in aggregate degree, ICT process and/or energy-transfer process for photophysical materials and organic electronic devices. As for **L**, a linear π-conjugated D-π-A type ICT molecule, the charge-transfer properties may be strongly influenced by the ordering degree of the molecules. A striking consequence of the different arrangements of **L** molecules in **L** square, **L** wire and/or **L** sphere is the disparity in the linear optical behavior for the three states, which can bring about the differences in the ground state and/or excited state dipole moment orientation, and further result in distinct optical features.

3.4.1. Absorption properties: The metal ion induced supramolecular aggregate of **L** wire and **L** sphere, which brought about not only the changes of morphology, but also differences in absorption properties. There also appeared two major absorption bands of **L** wire and/or **L** sphere, which were all red-shifted with different degrees from that of **L** square. The results indicated that the main π-conjugated chain and the triphenylamine fragment were affected during the metal ions participated aggregate procedure. As for **L** wires, two major absorption bands were centered at 312 nm and 450 nm, respectively.

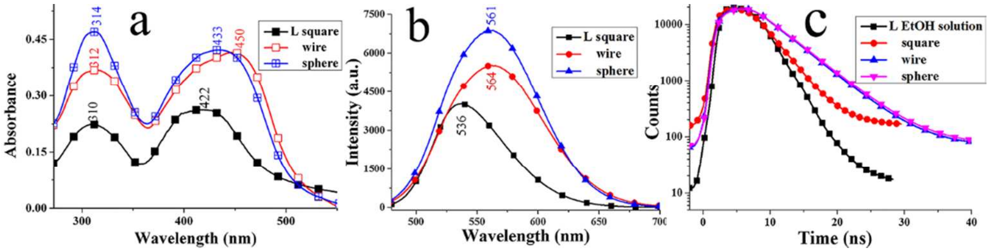

Figure 4 (a) UV-vis spectra; (b) fluorescence spectra; (c) time-domain fluorescence intensity of **L** square, **L** wire and **L** sphere, respectively.

For the latter, about 28 nm was red-shifted compared with that of **L** square (centered at 422 nm as shown in **Fig. 1b** and **4a**), while the and **L** components during the formation of **L** wires, which could enlarge the π-conjugated degree of **L** molecule and slightly affect the electron cloud distribution of triphenylamine group.

While for **L** spheres, two major absorption bands located at 314 nm and 433 nm, respectively. For the latter, about 11 nm red shifted compared with that of **L** square, while for the former, about 4 nm red shifted. The results meant that extent of tunable absorption spectrum was different under the existence of Cd^{2+} and Cu^{2+} ions, from which different enlarged π-conjugated degree of the whole molecule or absorption fragment was emerged. The phenomenon also revealed that the interaction 'hot spot' between Cu^{2+} ions and **L** molecules (which were not only through the π-conjugated chain of the whole molecule, but also the triphenylamine group) were different from that between Cd^{2+} ions and **L**. The results fit well with the observations discussed in SEM analysis, FT-IR and Raman studies mentioned above. As for **L** wires, the interactions between metal ions and the whole π-conjugated molecules may increase the ICT process and lead to the red-shift of the absorption. On the contrary, when Cu^{2+} ion was introduced, the interactions between Cu^{2+} and triphenylamine group (electron donor unit) of **L** may decrease the ICT process, while the interactions between Cu^{2+} ions and π-conjugated system/cyano group may increase the ICT. The combined effect resulted in a slightly red-shift absorption band [35] in this study. Thus, 28 nm red-shift of absorption band was observed for **L** wires, while only 11 nm red-shifted absorption band was appeared for that of Cu^{2+} ion. The red-shifted absorption of **L** wire and **L** sphere also revealed the aggregate degrees of combined metal ions were better than that of free **L** squares.

3.4.2. Fluorescent emission and FL lifetime: As discussed above, the fluorescence spectrum of free **L** square displayed a clear yellowish green emission centered at 536 nm (**Fig. 1c** and **4b**). The metal participated coupling, synergy effect and the corresponding supramolecular aggregation also resulted in enhanced fluorescence emission with different degrees. The brightest emission of **L** wires and/or **L** spheres in the EtOH-H_2O solution was captured at f_w = 99%, the f_w of which was higher than that of **L** square without the metal ions. Furthermore, as for **L** wires, the emission band red-shifted to 560 nm and the intensity enhanced for about 1.31 times from that of free **L** square with the fluorescence quantum yield increasing to 0.39. The fluorescence spectrum of **L** spheres centered at 560 nm, the intensity of which enhanced for about 1.75 times compared to that of **L** square with the fluorescence quantum yield being 0.51. The enhanced aggregation degree of **L** wires and/or **L** former red-shifted for only 2 nm from 310 nm of **L** square. The observation revealed the somewhat strong interactions between Cd^{2+} spheres, along with the energy transfer from **L** to metal ions [36], may be responsible for the red shifted spectra. The enhanced aggregation degree and/or the metal-to-ligand charge transfer (MLCT) [37] may be the main cause of the fluorescence enhancement. That was to say, the existence of metal ions changed not only the aggregate style, but also the electron distribution and excited state of **L** molecules. When Cd^{2+} and/or Cu^{2+} was in close contact with **L**, the electrostatic interactions between the organic and inorganic components affected the electron distribution of **L** molecules, which brought about electron redistribution of **L** and electricmagnetic coupling effect between the two components [38].

As for ICT type AIEE dyes, there are three types of mechanisms to change the emission intensity: aggregate degree, MLCT and ICT process. When metal ions were introduced into the organic matrix, energy transfer process may also influence the emission intensity. As discussed above, increased aggregate degree and/or MLCT process brought about enhanced emission in this study, while strong ICT process and energy transfer from **L** molecule to metal ion may give rise to fluorescence quenching. For **L** wires and **L** spheres, the influence of the aggregate degree and/or MLCT was the chief factor. Compared **L** wires with **L** spheres, the ICT process of **L** spheres was lower than that of **L** wires due to the interaction 'hot spot'. Thus, the emission intensity of **L** spheres was somewhat higher than that of **L** wires.

Time resolved fluorescence decay was employed to study the difference between the spectral features of **L** at three states. The average FL lifetime of **L** squares detected at 535 nm was 1.23 ns, which was somewhat higher than 1.01 ns of **L** in ethanol solution. The fluorescence of **L** squares was found to decay with two components, which indicated that there existed two kinds of fluorescent components. The result was in accordance with the two kinds of absorption bands (**Fig. 1b**, **4a**) and excitation bands (**Fig. S11**). A short component had a decay lifetime of 0.89 ns (the corresponding amplitude A = 90%), and the following component had 4.28 ns (10%), the results of which were very close to that of **L** molecules in ethanol solution as shown in **Table 1**. Meanwhile, for **L** wires and **L** spheres, the average FL lifetime detected at 560 nm was 1.56 ns and 1.75 ns (**Fig. 4c**), respectively, which was longer than that of **L** squares detected at 536 nm. The results revealed that **L** wires and/or **L** spheres seemed to provide a more stable environment for the excited state than **L** square. The increased average FL lifetime suggested that the existence of metal ions accelerated the yield of electron decay and/or lowered the rate of electron decay, which resulted in a longer average fluorescence decay lifetime [39]. Furthermore, the fluorescence of the **L** wires was decayed with three components. Compared with that of **L** squares, when **L** wires were detected at 560 nm, the corresponding amplitude (A) of a short component (0.74 ns) decreased from 90% to 67%. At the same time, a new component appeared with the fluorescence decay lifetime and the amplitude being 10.09 ns and 2%, respectively. The results confirmed the existence of a new fluorophore system in the **L** wires, as discussed previously. A similar phenomenon was also observed for **L** sphere, a new component appeared with the fluorescence decay lifetime and the amplitude being 10.84 ns and 5%, respectively, when **L** spheres were detected at 560 nm.

It is known that the FL lifetime of fluorophore is inversely proportional to the sum of the radiative decay rate (k^0_{rad}) and the nonradiative decay rate (k^0_{nr}) [40]. When metal ions are in close contact with the fluorophore, they can affect the intrinsic radiative and/or nonradiative decay rate of the fluorophore. In this study, enhanced emission of **L** wire and/or **L** sphere can also be attributed to the prolonged FL lifetime.

Table 1. Fluorescence decay lifetime (τ) and amplitude (A) of fluorescence of **L** square, **L** wire, **L** sphere and the corresponding energy transfer efficiency (ϕ_{ET})

Mater.	λ(nm)	τ1(ns)	A1(%)	τ2(ns)	A2(%)	τ3(ns)	A3(%)	$\overline{\tau}$ (ns)	χ^2	ϕ_{ET}(%)
L-EtOH solution	545	0.90	89	1.88	11	-	-	1.01	1.22	-
L square	536	0.89	90	4.28	10	-	-	1.23	1.66	-
L wire	535	0.56	75	2.16	23	8.79	2	1.06	1.44	13.8
	560	0.74	67	2.65	31	10.09	2	1.56	1.35	
L sphere	535	0.53	74	1.97	24	7.68	2	1.00	1.17	18.7
	560	0.82	65	2.25	30	10.84	5	1.75	1.24	

The energy transfer process between **L** molecule and metal ion was also studied from time resolved fluorescence experiment. As for **L** wires, the average FL lifetime detected at 535 nm was 1.06 ns, which was shorter than that of **L** squares detected at 536 nm. The result revealed the energy transfer process between the two components (that is to say, **L** molecule and metal ion) in the **L**. The energy transfer efficiency (ϕ_{ET}) [41] of **L**-Cd pair was estimated using **Equation (3)**.

$$\phi_{ET} = 1 - \frac{\tau_{wires}}{\tau_L} \quad (3)$$

where τ_{wire} was the average FL lifetime of **L** component in the **L** wires and τ_{L} was the average lifetime of free **L**. From these data, the estimated energy transfer efficiency in **L** wires was 13.8 %.

The energy transfer process was also detected for **L** spheres. The average FL lifetime of **L** component in **L** spheres detected at 535 nm was 1.00 ns, and the corresponding energy transfer efficiency (ϕ_{ET}) of **L** pair was calculated to be 18.7%. The somewhat stronger intermolecular interactions between **L** than that of **L** may be the main cause of the increased ϕ_{ET}.

3.5. Nonlinear optical properties

3.5.1 Two-photon absorption (2PA) and two-photon excited fluorescence (2PEF): Except for the appearance of the tunable linear optical properties, the interactions between metal ion and **L** molecule, the corresponding changeable growth direction, increased aggregate degree, changeable ICT process also resulted in significant difference of 2PA and 2PEF. **Fig. S20** showed log-log plot of the excited fluorescence signal *vs* excited light power. The slope was 2.004 for **L** squares, 1.989 for **L** wires and 1.977 for **L** spheres, respectively, which provided direct evidence for two-photon excited process. The best 2PA wavelength obtained from Z-scan experiments was 840 nm for **L** squares, 860 nm for **L** wires and 840 nm for **L** spheres as shown in **Fig. 5a**.

The 2PEF spectra of the three samples were shown in **Fig. 5b**, respectively. The emission maxima located at 588 nm for **L** squares, 595 nm for **L** wires and 594 nm for **L** spheres, respectively. The enlarged aggregate degree, the enlarged π-conjugated system caused from **L**-metal interactions through π-conjugated units, and the increased ICT process may bring about the red-shifted 2PEF of **L** wires, **L** spheres compared with that of **L** squares. Furthermore, the 2PEF peak position of the samples showed a red-shift with different extent compared to that of SPEF (see **Fig. 4b**), which was 52 nm red-shift for **L** squares, 31 nm for **L** wire and 33 nm for **L** spheres, respectively. Also, the 2PEF intensity exhibited an increase for about 1.38 times from **L** squares to **L** wires and ~60% decrease to **L** spheres. The results indicated the difference of the excited states for SPEF and 2PEF, mainly during the excitation process: two-photon absorption *vs* single-photon absorption [42].

There are two factors to influence the 2PEF intensity. One is the enhanced aggregate degree of **L** molecules and/or enlarged π-conjugated system which may increase the 2PEF intensity [43]. The other is the scattering phenomenon [26, 44] that caused from the large particles, which may result in quenched 2PEF, along with the heavy atom effect [45]. As for **L** wires, the enhanced 2PEF revealed that the increased aggregate degree of **L** molecules, the enlarged π-conjugated system will be the main cause of the enhancement. As for **L** sphere, the heavy atom effect and the scattering phenomenon may be the dominant factor.

3.5.2. Open Z-scan experiment: Open aperture Z-scan experiments were carried out using femtosecond laser pulse to investigate nonlinear optical (NLO) properties of the three samples, and the results are shown in **Fig. 5c**. The best input laser wavelength determined from Z-scan experiments was 840 nm for **L** square, 860 nm for **L** wire and 840 nm for **L** sphere, respectively. All of the Z-scan curves displayed a decrease in transmittance at the focal point of the laser, which was typical of a positive NLO effect. The minimum transmittances at Z = 0 were 97, 95.6, and 46.8% for the **L** square, **L** wire, and **L** sphere, respectively. The transmittance curves of the **L** square and **L** wire were quite similar to each other, and the NLO performance of **L** sphere was obviously better than that of the other two. Moreover, **L** sphere had the largest decrease in transmittance of the three samples, indicating that optical absorbance enhancement was achieved with the participation of Cu^{2+} ions.

Based on the **Equation 1** (shown in Experimental Section), the 2PA coefficient β of **L** square was calculated to be 0.01075 cm/GW, which was 0.01524 cm/GW for **L** wire and 0.06102 cm/GW for **L** sphere, respectively. Obviously, the β of the metal ions participated aggregates were larger than that without metal ions. Enlarged aggregate degree and strong electron coupling effects made significant contribution to the enhancement of the 2PA coefficient. Based on **Equation 2**, the calculated 2PA cross section δ was 486.00 GM (1 GM = 10^{-50} cm^4 s $photon^{-1}$) for **L** square, which increased to 661.92 GM for **L** wire, and increased sharply for about 6 times to 2721.62 GM for **L** sphere. The uncertainty in the experimental δ values is estimated to be ±15%. There are two factors to influence the 2PA cross-section. Firstly, the enlarged π-conjugated degree and the corresponding metal participated ordering aggregates of **L** molecules may increase the 2PA cross-section. Secondly, the large particles may result in scattering phenomenon and decreased 2PA cross-section. As for this study, the increased data of δ revealed that the enlarged π-conjugated degree, increased aggregates of **L** molecules and the corresponding increased molecular number density of 2PA active **L** molecules will be the main cause of the enhancement.

Furthermore, the enlarged δ of **L** sphere than that of **L** wire further indicated the stronger intermolecular interactions in **L** sphere than that in **L** wire, which fit well with the discussions mentioned above. Here, comparing to hard preparation of complicated organic fluorophore with large δ value, we prefer to the facile and high-yield synthesis of metal participated ordered aggregates to show better photophysical properties. In the as-prepared metal ions participated aggregates, the metal ions can serve either as a multidimensional template for increasing the molecular number density of 2PA active component (**L**) and increasing the π-conjugated system, or as an important part of the structure to control the intramolecular charge-transfer and/or effective intermolecular energy transfer process, leading to an enhanced δ value.

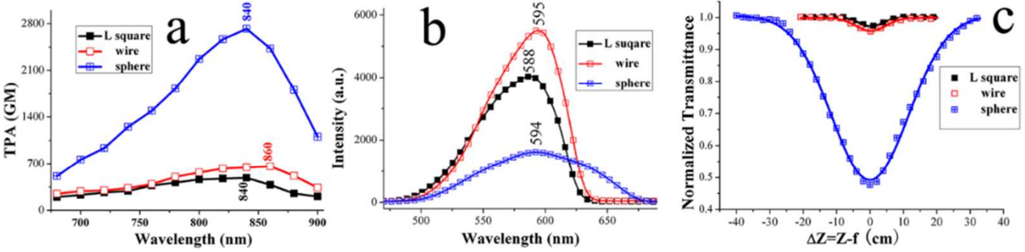

Figure 5 a) 2PA spectra, b) 2PEF spectra, and c) Open Z-scan experiments of **L** square, **L** wire and **L** sphere, respectively.

Moreover, it was found that the δ_{2PA} values of the three samples were all larger than that of many fluorophore widely used in biology, such as fluorescein, BODIPY, GFP, and so on [46], which were of considerable interest, indicating the potential application in bioimaging. For applications, the molecules with large 2PA action cross section (ηδ) are needed. As for the studied three samples, the ηδ value was 160 GM for **L** square, 258 GM for **L** wire and 1388 GM for **L** sphere, respectively. The data revealed that the three samples were all suitable for potential application in two-photon microscopy biological imaging.

3.6. Two-photon microscopy bio-imaging application

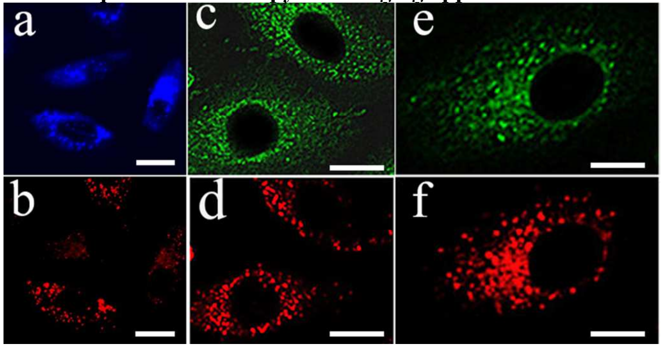

Figure 6 (a), (c) and (e): One-photon image of HepG2 cells incubated with 20 μM **L** square, **L** wire and **L** sphere, respectively, after 30 min of incubation, washed by PBS buffer; (b), (d) and (f): Two-photon image of HepG2 cells incubated with 20 μM of **L** square, **L** wire and **L** sphere, respectively, after 30 min of incubation, washed by PBS buffer. Scale bar = 20 μm.

To evaluate the performance of the as-prepared aggregates in live cells, a 2PFM imaging and a cytotoxicity analysis were conducted [47]. HepG2 cells (human liver cancer cell) were the testing candidates, cultured and stained with the three samples [48]. Considering the application in 2PMF imaging, as the particle has to be smaller enough to penetrate plasma membrane and internalise with subcellular organelle, therefore the three samples were firstly ultrasonic dispersed in 10% PBS solution for 10 min, then the samples were left undisturbed and some larger particles were precipitated naturally. Later the upper solutions, among which the size was much smaller, were diluted by PBS to certain concentrations and then used to study the 2PMF imaging. The morphology of the samples in upper solution (ESI† **Fig. S22**) were similar to that shown in **Fig. 1** and **3**. Meanwhile, the size of the three samples were smaller than that before sonication treatment. The size of pure **L** was about 100 nm, which was ~2 μm long and ~50 nm wide for **L** wire, and ~70 nm large for **L** spheres, respectively.

MTT assay was performed to ascertain the cytotoxicity of the three samples against HepG2 cell over a 24 h period [49]. **Fig. S24** showed that the cell viability treated with three samples at different concentrations for 24 h. The results suggested good biocompatibility of **L** aggregates at such formulation, as Cd^{2+} and Cu^{2+} are the essential trace elements in human body, and these ions with low concentration are nontoxic and/or low-toxic to human cells *in vitro*. The cytotoxicity tests showed that sub- and low-micromolar concentrations of the samples would not produce obvious toxic effects on living cells over a period of 24 h, hence the samples could safely be used for further biological studies.

The stability of metal embedded organic nanostructures in cell media, especially whether the metal ions release from the structure, is very important before the bio-application experiments. Thus, prior to the investigations on bioimaging in living cells for the samples undertaken, the stability of the particles in living cells was studied. The fluorescence emission of the samples in the HepG2 cell media was studied. The results revealed that the relative intensity and emission band of the fluorescence were similar to that out of the cell media (**Fig. S25**), showing the stability of the samples in the cell culture media.

The large 2PA action cross-sections, relative low cytotoxicity in low concentration of these samples and stability of them in cell culture media made them attractive candidates as two-photon imaging agents. Two-photon excitation cell imaging using **L** square, **L** wire, and **L** sphere were achieved by using HepG2 cancer cells with a two-photon laser scanning confocal microscopy (**Fig. 6**).

Treated cells were excited at proper 2PA wavelength, which was 840 nm for **L** square, 860 nm for **L** wire and 840 nm for **L** sphere, respectively.

The blue channel in **Fig. 6a**, the green channel in **Fig. 6c** and **e** showed 1PFM imaging. The red channels in **Fig. 6b**, **d** and **f** showed 2PFM imaging. These micrographs clearly revealed that the samples successfully internalised with HepG2 cells. Two-photon induced fluorescence was observed predominantly from the cellular cytoplasmic region, which was consistent with the images collected *via* 1PFM imaging.

For **L** square, the confocal micrograph (**Fig. 6a-b**) of each live cell were successfully taken and clearly showed endosomal/ lysosomal like interactions. Presumably the luminescence came from **L** square penetrated the phospholipids bilayers of cell membrane into the cytoplasm, and accumulated beyond/within lysosome. The result suggested that **L** might internalise with cells *via* clathrin-dependent endocytosis (receptor mediated endocytosis). Interestingly, both for **L** wire and **L** sphere, the confocal micrograph (**Fig. 6c-f**) showed endosomal/ intercellular substance like interaction, the samples uptake all around the intercellular substance, not only lysosome but also mitochondrion [50]. The cell-permeability for mitochondrial imaging of the two samples (**L** wire and **L** sphere) accounted for the existence of metal ions. The metal ions of **L** wires and/or **L** spheres can strengthen the interactions between the proteins of intercellular substance (mitochondrion and lysosome included) and **L** wires/spheres, which may further bring about the uptaking all around the intercellular substance. The phenomena further revealed that the bio-imaging application scope of two metal ion-participated aggregates was more extensive than that without metal ions.

In addition, the **L** wire and **L** sphere in HepG2 intercellular substance region revealed 2PEF stability and almost no photobleaching upon laser irradiation (ESI†, **Fig. S27**). The record 2PA coefficient and its application for in *vivo* 2PFM imaging highlighted the potential of the metal participated self-assembly organic aggregates.

The results of the 2PFM imaging revealed that metal ions participated **L** aggregates were cell-permeable and suitable for the cytosol staining, and exhibited the high 2PEF sensitivity in live cells and that they were clearly capable of detecting the intercellular substance section in HepG2 cells. The current results suggested metal ions participated self-aggregates could enlarge the repertoire of the biomolecular target specificity.

4. Conclusion

In summary, a facile mechanism was studied for assembling a D-π-A type organic molecule (**L**), endowing with intramolecular charge transfer (ICT) feature and AIEE properties, into long-range ordered organization that could bridge length scales from nanometers to macroscopic dimensions under the guidance of metal ions (Cd^{2+} and/or Cu^{2+}). Self-aggregate of **L** molecules from $EtOH-H_2O$ mixed solvent showed square-like morphology, which revealed wire-like shape under the guidance of Cd^{2+} ions and spheres were observed when Cu^{2+} ion was used, respectively. Along with the morphological variation, energy-transfer process between **L** and metal ions emerged, which resulted in red-shifted linear optical properties, enhanced fluorescent quantum yield along with changeable FL lifetime, enlarged two-photon action cross section and enhanced 2PA coefficient. The as-prepared self-aggregates exhibit successful application to a two-photon fluorescent probe for labeling the intercellular substance section (mitochondrion and lysosome included) in HepG2 cells. We envisage that this enlarged self-aggregate approach is general and shall be extended to the fabrication of a wide range of multifunctional nanomaterials by judicious selection of the chromophore, metal component, and reaction mediums, which may be used for a multitude of photonic and/or optoelectronic applications in bio- and chemical sensing and nanoelectronics employing its photosensitive, energy transfer and synergy effect.

Acknowledgements

This work was supported by the NSFC (No: 21271004, 51372003, 21101001), Educational Commission of Anhui Province of China (KJ2014D02), The 211 Project of AnHui University (02303319).

Notes and references

[a] Department of Chemistry, Key Laboratory of Inorganic Materials Chemistry of Anhui Province, Anhui University, Hefei 230039, (P.R. China).
[b] State Key Laboratory of Crystal Materials, Shandong University, Jinan, P. R. China.
[c] State Key Laboratory of Coordination Chemistry, Nanjing University, Nanjing 210093, P. R. China
*Corresponding author. Fax: +86-551-63861279; Tel: +86-551-63861279;
E-mail address: yptian@ahu.edu.cn, jxyang@ahu.edu.cn

† CCDC 967699 contains the supplementary crystallographic data for this paper. These data can be obtained free of charge from The Cambridge Crystallographic Data Centre via www.ccdc.cam.ac.uk/data_request/cif.

Electronic Supplementary Information (ESI) available: [Selected bond length and bond angles of **L**; The 1-D and 2-D framework diagram of **L**; SEM images; FT-IR spectra; Determination of metal ions embedded in **L** matrix; Photostability and thermal stability; Morphology and size distribution of the particles used in bioimage; Calculated frontier orbital **L** in the gas phase; Some of calculated excitation energies (E), oscillator strengths (f), corresponding wavelengths (λ_{abs} and λ_{em}) and major contributors for **L**; Non-linear optical measurements; 1PFM and 2PFM images.]. See DOI: 10.1039/b000000x/

1 a) Q. Zhang, L. Li, M. Zhang, Z. D. Liu, J. Y. Wu, H. P. Zhou, J. X. Yang, S. Y. Zhang, Y. P. Tian, ***Dalton Trans***., 2013, **42**, 8848; b) M. S. Steiner, A. Duerkop and O. S. Wolfbeis, ***Chem. Soc. Rev***., 2011, **40**, 4805.

2 D. R. Larson, W. Zipfel, R. M. Williams, S. W. Clark, M. P. Bruchez, F. W. Wise, W. W. Webb, *Science*, 2003, **300**, 1434.

3 a) R. Piner, J. Zhu, F. Xu, S. Hong, C. Mirkin, *Science*, 1999, **283**, 661; b) L. Kong, J. X. Yang, S. L. Li, Q. Zhang, Z. X. Xue, H. P. Zhou, J. Y. Wu, B. K. Jin, Y. P. Tian, *Chem. Eur. J.*, 2013, **19**, 16625.

4 J. L. Geng, K.i Li, D. Ding, X. H. Zhang, W. Qin, J. Z. Liu, B. Z. Tang, B. Liu, *Small* 2012, **8**, 3655.

5 a) Y. H. Jiang, Y. C. Wang, J. L. Hua, J. Tang, B. Li, S. X. Qian, H. Tian, *Chem. Commun.*, 2010, **46**, 4689; b) Y. H. Jiang, Y. C. Wang, B. Wang, J. B. Yang, N. N. He, S. X. Qian, J. L. Hua, *Chem. Eur. J.*, 2011, **17**, 2479.

6 a) G. S. He, L. H. Tan, Q. D. Zheng, P. N. Prasad, *Chem. Rev.* 2008, **108**, 1245; b) T. C. He, R. Chen, Z. B. Lim, D. Rajwar, L. Ma, Y. Wang, Y. Gao, A. C. Grimsdale, H. D. Sun, *Adv. Optical Mater.*, 2014, **2**, 40; c) M. H. Lee, J. H. Han, J. H. Lee, N. Park, R. Kumar, C. Kang, J. S. Kim, *Angew. Chem. Int. Ed.*, 2013, **52**, 6206; d) S. Huang, L. Y. Zou, A. M. Ren, J. F. Guo, X. T. Liu, J. K. Feng, B. Z. Yang, *Inorg. Chem.*, 2013, **52**, 5702; e) K. Kamada, S. Fuku-en, S. Minamide, K. Ohta, Y. Yamamoto, *J. Am. Chem. Soc.*, 2013, **135**, 232; f) T. C. Lin, Y. H. Lee, C. Y. Liu, B. R. Huang, J. H. Lin, *Chem. Eur. J.*, 2013, **19**, 749; g) B. J. Xu, M. Y. Xie, Z. G. Chi, F. L. Zhao, *Chem. Commun.*, 2013, **49**, 273.

7 a) Y, L. Lu, W. Chen, *Chem. Soc. Rev.*, 2012, **41**, 3594; b) L. Shang, S. J. Dong, G. U. Nienhaus, *Nano Today*, 2011, **6**, 401; c) P. Yuan, R. Ma, Z. Guan, N. Gao, and Q. H. Xu, *ACS Appl. Mater. Interfaces*, 2014, **6**, 13149; d) H. H. Mai, V. E. Kaydashev, V. K. Tikhomirov, E. Janssens, M. V. Shestakov, M. Meledina, S. Turner, G. V. Tendeloo, V. V. Moshchalkov, P. Lievens, *J. Phys. Chem. C*, 2014, **118**, 15995.

8 L. Li, Y. P. Tian, J. X. Yang, P. P. Sun, J. Y. Wu, H. P. Zhou, S. Y. Zhang, B. K. Jin, X. J. Xing, C. K. Wang, M. Li, G. H. Cheng, H.

H.Tang, W. H. Huang, X. T. Tao, M. H. Jiang, *Chem. Asian J.*, 2009, **4**, 668.

9 a) C. T. Chen, *Chem. Mater.*, 2004, **16**, 4389; b) S. W. Tomas, G. D. Joly and T. M. Swager, *Chem. Rev.*, 2007, **107**, 1339;

10 J. D. Luo, Z. L. Xie, J. W. Y. Lam, L. Cheng, H. Y. Chen, C. F. Qiu, H. S. Kwok, X. W. Zhan, Y. Q. Liu, D. B. Zhu, B. Z. Tang, *Chem. Commun.*, 2001, 1740;

11 a) G. F. Zhang, Z. Q. Chen, M. P. Aldred, Z. Hu, T. Chen, Z. Huang, X. G. Meng, M. Q. Zhu, *Chem. Commun.*, 2014, DOI: 10.1039/c4cc04241g; b) W. B. Jia, H. W. Wang, L. M. Yang, H. B. Lu, L. Kong, Y. P. Tian, X. T. Tao, J. X. Yang, *J. Mater. Chem. C*, 2013, **1**, 7092; c) H. Tong, Y. Dong, Y. Hong, M. Häussler, J. W. Y. Lam, H. H.-Y. Sung, X. Yu, J. Sun, I. D. Williams, H. S. Kwok, B. Z. Tang, *J. Phys. Chem. C* 2007, **111**, 2287; d) Z. Li, Y. Dong, B. Mi, Y. Tang, M. Häussler, H. Tong, Y. Dong, J. W. Y. Lam, Y. Ren, H. H. Y. Sung, K. S. Wong, P. Gao, I. D. Williams, H. S. Kwok, B. Z. Tang, *J. Phys. Chem. B* 2005, **109**, 10061.

12 a) K. Li, Y. H. Jiang, D. Ding, X. H. Zhang, Y. T. Liu, J. L. Hua, S. S. Feng, B. Liu, *Chem. Commun.*, 2011, **47**, 7323;

13 J. Wang, J. Mei, R. R. Hu, J. Z. Sun, A. J. Qin, B. Z. Tang, *J. Am. Chem. Soc.,* 2012, **134**, 9956.

14 X. Zhang, D. Gçrl, V. Stepanenko, F. Würthner, *Angew. Chem.*, 2014, **126**, 1294.

15 B. K. An, S. H. Gihm, J. W. Chung, C. R. Park, S. K. Kwon, S. Y. Park, *J. Am. Chem. Soc.*, 2009, **131**, 3950.

16 P. Y. Gu, C. J. Lu, Z. J. Hu, N. J. Li, T. T. Zhao, Q. F. Xu, Q. H. Xu, J. D. Zhang, J. M. Lu, *J. Mater. Chem. C*, 2013, **1**, 2599.

17 F. Stellacci, C. A. Bauer, T. Meyer-Friedrichsen, W. Wenseleers, S. R. Marder, J. W. Perry, *J. Am. Chem. Soc.*, 2003, **125**, 328.

18 Y. J. Li, T. F. Liu, H. B. Liu, M. Z. Tian, Y. L. Li, *Acc. Chem. Res.*, 2014, **47**, 1186.

19 R. Dutta, P. Ghosh, *Chem. Commun.*, 2014, **50**, 10538.

20 H. Xu, J. Penfold, R. K. Thomas, J. T. Petkov, I. Tucker, J. R. P. Webster, I. Grillo, A. Terry, *Langmuir*, 2014, **30**, 4694.

21 G. F. Zhang, M. P. Aldred, W. L. Gong, C. Li, M. Q. Zhu, *Chem. Commun*., 2012, **48**, 7711.

22 a) E. Wei, B. Liu, S. Lin, F. Liang, *Org. Biomol. Chem.*, 2014, **12**, 6389; b) S. Lin, Y. Wei, F. Liang, *Chem. Commun.*, 2012, **48**, 9879.

23 G. M. Sheldrick, SHELXTL V5.1 Software Reference Manual, Bruker, AXS Inc., Madison, Wisconsin, USA, 1997.

24 L. Kong, J. X. Yang, H. P. Zhou, S. L. Li, F. Y. Hao, Q. Zhang, Y. L. Tu, J. Y. Wu, Z. M. Xue, Y. P. Tian, *Sci. China Chem*., 2013, **56**, 106.

25 a) W. I. Gruszecki, *J. Biol. Phys.*, 1991, **18**, 99; b) S. Gadde, E. K. Batchelor, J. P. Weiss, Y. Ling, A. E. Kaifer, *J. Am. Chem. Soc.*, 2008, **130**, 17114.

26 M. Retsch, M. Schmelzeisen, H. J. Butt, E. L. Thomas, *Nano Lett.*, 2011, **11**, 1389.

27 a) Y. Li, L. Xu, T. Liu, Y. Yu, H. Liu, Y. Li, D. Zhu, *Org. Lett.*, 2011, **13**, 5692; b) W. Qin, D. Ding, J. Liu, W. Z. Yuan, Y. Hu, B. Liu, B. Z. Tang, *Adv. Funct. Mater.* 2012, **22**, 771; c) W. Z. Yuan, Y. Gong, S. Chen, X. Y. Shen, J. W. Y. Lam, P. Lu, Y. Lu, Z. Wang, R. Hu, N. Xie, H. S. Kwok, Y. Zhang, J. Z. Sun, B. Z. Tang, *Chem. Mater.*, 2012, **24**, 1518

28 a) L. J. Qian, B. Tong, J. B. Shen, J. B. Shi, J. G. Zhi, B. Z. Tang, *J. Phys. Chem. B*, 2009, **113**, 9098; b) W. Z. Yuan, X. Y. Shen, H. Zhao, J. W. Y. Lam, L. Tang, B. Z. Tang, *J. Phys. Chem. C*, 2010, **114**, 6090; c) C. M. Yang, I. W. Lee, T. L. Chen and J. L. Hong, *J. Mater. Chem. C*, 2013, **1**, 2842; d) Y. L. Cao, M. D. Yang, Y. Wang, H. P. Zhou, J. Zheng, X. Z. Zhang, J. Y. Wu, Y. P. Tian, Z. Q. Wu, *J. Mater. Chem. C*, 2014, **2**, 3686.

29 Z. Y. Yang, Z. G. Chi, T. Yu, X. Q. Zhang, M. N. Chen, B. J. Xu, S. W. Liu, Y. Zhang, J. R. Xu, *J. Mater. Chem.*, 2009, **19**, 5541.

30 C. Y. K. Chan, Z. J. Zhao, J. K. Y. Lam, J. Z. Liu, S. M. Chen, P. Lu, F. Mahtab, X. J. Chen, H. H. Y. Sung, H. S. Kwok, Y. G. Ma, I. D. Williams, K. S. Wong, B. Z. Tang, *Adv. Funct. Mater.*, 2012, **22**, 378.

31 S. R. Marder, D. N. Beratan, L. T. Cheng, *Science* 1991, **252**, 103; H. Wang, Q. Zhang, J. Zhang, L. Li, Q. Zhang, S. L. Li, S. Y. Zhang, J. Y. Wu, Y. P. Tian, *Dyes and Pigments* 2014, **102**, 263.

32 M. Muniz-Miranda, B. Pergolese, A. Bigotto, *J. Phys. Chem. C* 2008, **112**, 6988

33 Y. L. Wang, D. Li, P. C. Li, W. D. Wang, W. Ren, S. J. Dong, E. K. Wang, *J. Phys. Chem. C* 2007, **111**, 16833.

34 X. G. Hu, T. Wang, L. Wang, S. J. Dong, *J. Phys. Chem. C* 2007, **111**, 6962.

35 A. Bhaskar, G. Ramakrishna, R. J. Twieg, T. Goodson, III, *J. Phys. Chem. C* 2007, **111**, 14607.

36 a) M. H. Stewart, A. L. Huston, A. M. Scott, E. Oh, W. R. Algar, J. R. Deschamps, K. Susumu, V. Jain, D. E. Prasuhn, J. Blanco-Canosa, P. E. Dawson, I. L. Medintz, *ACS Nano*, 2013, **7**, 9489; b) J. Liu, Y. Liu, X. Yang, K. Wang, Q. Wang, H. Shi, L. Li, *Anal. Chem.* 2013, **85**, 11121

37 W. L. Gong, M. P. Aldred, G. F. Zhang, C. Li, M. Q. Zhu, *J. Mater. Chem. C*, 2013, **1**, 7519

38 a) K. Hanaoka, Y. Muramatsu, Y. Urano, T. Terai, T. Nagano, *Chem. Eur. J.* 2010, **16**, 568; b) L. Kong, J. X. Yang, X. P. Hao, H. P. Zhou, J. Y. Wu, F. Y. Hao, L. Li, S. Y. Zhang, B. K. Jin, X. T. Tao, M. H. Jiang, Y. P. Tian, *J. Mater. Chem.* 2010**, 20**, 7372.

39 a) J. E. Yarnell, J. C. Deaton, C. E. McCusker, F. N. Castellano, *Inorg. Chem.*, 2011, **50**, 7820; b) S. Murphy, L. Huang, P. V. Kamat, *J. Phys. Chem. C*, 2011, **115**, 22761.

40 K. S. Kim, J. H. Kim, H. Kim, F. Laquai, E. Arifin, J. K. Lee, S. I. Yoo, B. H. Sohn, *ACS Nano*, 2012, **6**, 5051.

41 a) A. Panáčk, L. Kvítek, R. Prucek, M. Kolář, R.Večeřov, N. Pizúrová, V. K. Sharma, T. Nevěčná, R. Zboáil, *J. Phys. Chem. B*, 2006, **110**, 16248; b) T. L. Jennings, M. P. Singh, G. F. Strouse, *J. Am. Chem. Soc.*, 2006, **128**, 5462.

42 P. Milosz, A. C. Hazel, G. D. Robert, L. A. Harry. *Angew. Chem. Int. Ed.* 2009, **48**, 3244.

43 L. Li, Y. P. Tian, J. X. Yang, P. P. Sun, L. Kong, J. Y. Wu, H. P. Zhou, S. Y. Zhang, B. K. Jin, X. T. Tao, M. H. Jiang, *Chem. Commun.* 2010, **46**, 1673.

44 H. Auweter, H. Haberkorn, W. Heckmann, D. Horn, E. Lüddecke, J. Rieger, H. Weiss, *Angew. Chem., Int. Ed.*, 1999, **38**, 2188.

45 a) P. S. Skell, S. J. Valenty, P. W. Humer, *J. Am. Chem. Soc.* **1973**, ***95***, 5041; b) A. R. Gutierrez, D. G. Whitten, *J. Am. Chem. Soc.* **1974**, ***96***, 7128.

46 a) J. J. Chen, P. Zhao, H. B. Lv, Y. Yu, P. Y. Xu, *Chem. Commun.* 2011, **47**, 2435; b) A. Picot, A. D'Aléo, P. L. Baldeck, A. Grichine, A. Duperray, C. Andraud, O. Maury, *J. Am. Chem. Soc.* 2008, **130**, 1532; c) N. Rendón, A. Bourdolle, P. L. Baldeck, H. Le Bozec, C. Andraud, S. Brasselet, C. Coperet, O. Maury, *Chem. Mater.* 2011, **23**, 3228.

47 a) H. M. Kim, B. R. Cho, *Acc. Chem. Res.* 2009, **42**, 863; b) P. C. Zhang, A. G. Cheetham, L. L. Lock, H. Cui, *Bioconjugate Chem.* 2013, **24**, 604.

48 S. J. Yu, J. B. Chao, J. Sun, Y. G. Yin, J. F. Liu, G. B. Jiang, *Environ. Sci. Technol.* 2013, **47**, 3268.

49 H. Y. Ahn, K. E. Fairfull-Smith, B. J. Morrow, V. Lussini, B. Kim, M. V. Bondar, S. E. Bottle, K. D. Belfield, *J. Am. Chem. Soc.* 2012, **134**, 4721.

50 a) M. Gao, C. K. Sim, C. W. T. Leung, Q. L. Hu, G. X. Feng, F. Xu, B. Z. Tang, B. Liu, *Chem. Commun.*, 2014, **50**, 8312; b) C. W. T. Leung, Y. Hong, S. Chen, E. Zhao, J. W. Y. Lam, B. Z. Tang, *J. Am. Chem. Soc.*, 2013, **135**, 62.

Graphical abstract for:

Self-assembly of metal ions induced highly emissive fluorophore-triphenylamine nanostrctures: enhanced two-photon action cross section for bioimaging applications

Lin Kong, Yu-peng Tian*, Qi-yu Chen, Qiong Zhang, Hui Wang, Dong-qin Tan, Zhao-ming Xue, Hong-ping Zhou, Jie-ying Wu, Jia-xiang Yang*

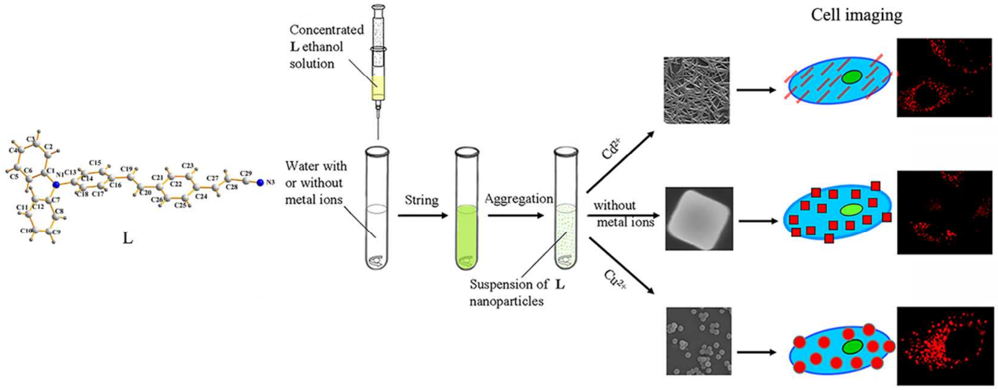

Metal induced self-aggregate of an AIEE type TPA material enhanced the two-photon action cross section for bioimage in HepG2 cells.